ACS APPLIED ENERGY MATERIALS

www.acsaem.org Article

Enhanced Thermoelectric Properties of Electrodeposited Cu-Doped Te Films

Swatchith Lal, Kafil M. Razeeb,* and Devendraprakash Gautam*

Cite This: https://dx.doi.org/10.1021/acsaem.9b02153 Read Online

ACCESS | Metrics & More | Article Recommendations | Supporting Information

ABSTRACT: Bismuth telluride-based alloys are the best-known thermoelectric materials in the room-temperature regime. Here, we report on the enhanced thermoelectric properties of electrodeposited copper-doped tellurium films as an n-type thermoelectric material for near-room-temperature applications. With the increase of the copper content in the films, we observe an enhancement of the thermoelectric properties. Thereby, we investigate the role of copper in modifying the crystal structure, which leads to the amorphous nature of the films and the corresponding enhancement in the thermoelectric properties. The electrodeposited copper-doped tellurium films exhibit a high Seebeck coefficient of −227 μV/K, resulting to a power factor of 5.6 mW/mK^2, which is a promising power factor observed for the electrodeposited thermoelectric materials and can be a favorable n-type thermoelectric material for device applications.

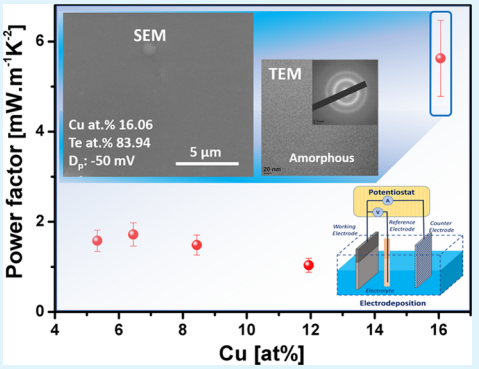

KEYWORDS: *thermoelectric material, electrodeposition, power-factor, energy harvesting, Cu-doped Te thin films*

1. INTRODUCTION

The advancement in electronics and the constant drive for miniaturization have given rise to a highly integrated system but opened up the challenge of managing the thermal budget of these integrated systems. Simultaneously, in the era of the internet of things (IoT),[1−4] low-power-consuming wireless sensor nodes (typically in the range of milliwatts to microwatts) that enable to create a smarter and more responsive environment are required. Typically, batteries employed to power up these sensor nodes fail and need to be replaced after a limited time, which adds up to the cost.[3,5] Therefore, power generation from abundant waste heat using thermoelectric (TE) materials is receiving huge attention by researchers both in the academia and industry.[6,7] A TE device can transform thermal energy into electricity using the "Seebeck effect" and conversely enable cooling or heating using the "Peltier effect". Microscale TE devices have huge advantages over macroscopic devices. The apparent advantage is the smaller size, which allows integration into compact, smaller systems. Due to the use of small structures, the integration density increases, thereby significantly increasing the number of thermocouples in the device, leading to high power outputs, especially for small temperature differences.[8,9] The present state-of-the-art micro-thermoelectric generators (μTEG) are mainly fabricated using silicon fabrication technology and microelectromechanical system (MEMS)-compatible techniques. These techniques are the basis of many rapidly growing technologies because they combine miniaturized sensors and actuators with electronics, resulting in a substantial reduction in the device cost.[10,11]

Another challenge to address is to synthesize a highly efficient thermoelectric material. Bi_2Te_3-based thermoelectric materials still dominate the room temperature applications.[12−15] However, copper-based TE materials, such as copper selenide,[16] copper sulfide,[17,18] and copper telluride,[19] are getting renewed attention[20] as they exhibit excellent TE efficiency. It is worth mentioning that all these copper-based TE materials are bulk materials exhibiting a p-type behavior, and their working temperature are around ∼700−900 K.[20] So far, all Cu-based thermoelectric materials reported in the literature demonstrated a high TE performance at the high-temperature regime. Here, we report the development of Cu-doped Te films for thermoelectric applications near room temperature. We synthesize Cu-doped Te films using electrodeposition and characterize structural and TE properties of the as-deposited materials. The role of Cu on the crystal structure of the Te film and its effect on the thermoelectric properties are discussed in detail. The excellent thermoelectric properties exhibited by Cu-doped Te films can lead to a potential thermoelectric material for power generation in near-room-temperature applications, specifically for low differential temperature scenarios.

Received: November 6, 2019
Accepted: April 2, 2020
Published: April 2, 2020

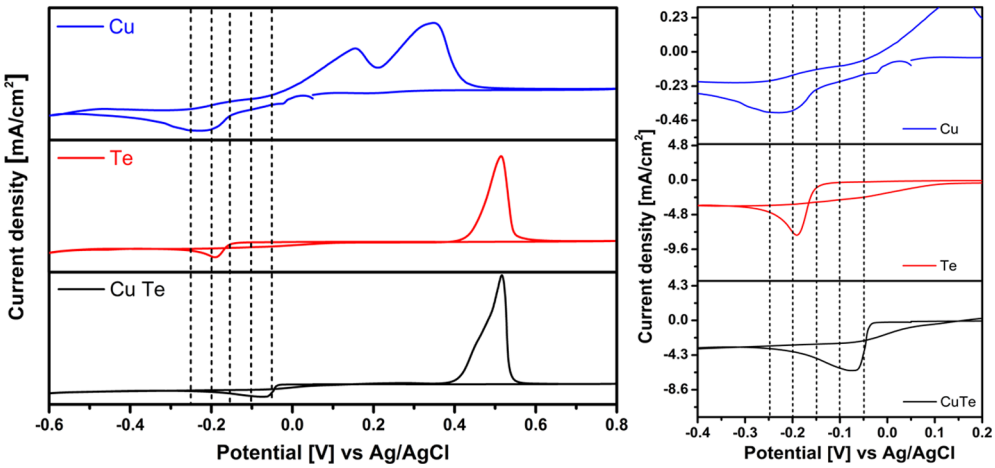

Figure 1. Cyclic voltammogram recorded on a standard gold working electrode in the Cu, Te, and CuTe electrolytes, and a magnified image of reduction peaks (right).

A great deal of work in enhancing the figure of merit (ZT) of the material has been carried out and reported in the literature over the last decade.[14,21−24] The maximum power density of a thermoelectric device is closely associated with the power factor of the thermoelectric materials. Higher power factors lead to larger output power densities for a given working condition.[25,26] Developing thermoelectric materials with a high power factor is crucially important for real-time applications. Here, we also report the extraordinary power factor exhibited by Cu-doped Te film for room-temperature application, which is at par with the highest power factor reported for a thin-film thermoelectric material developed by electrodeposition so far.[27−29]

2. EXPERIMENTAL SECTION

All the depositions were performed at room temperature from an electrolyte containing 1 M nitric acid, 15 mM pure tellurium powder, and 2 mM copper (II) sulfate pentahydrate. In order to prepare the solution, tellurium was first dissolved in 1 M nitric acid and heated at 40 °C while stirring. Copper (II) sulfate pentahydrate was separately dissolved in deionized (DI) water. Both the solutions were mixed at a later stage while stirring to form the final solution. Cyclic voltammetry (CV) was performed using a standard gold electrode with respect to the Ag/AgCl reference electrode at a sweep rate of 10 mV s^{-1}. A platinized titanium mesh was used as the counter electrode. The thermoelectric films were electrodeposited on a Si/SiO_2 substrate, having 20 nm of gold (Au) layer on top of the 10 nm titanium (Ti) adhesion layer. All the depositions were performed for 1 h at room temperature by applying different deposition potentials (−50 to −250 mV). The deposition area of the sample was fixed to 9 cm^2. All the samples were rinsed using DI water and with isopropanol and again with DI water before drying under a nitrogen jet.

Morphology of the films was observed using scanning electron microscopy (SEM) (Quanta FEG 450), and the composition was determined with energy-dispersive X-ray spectroscopy (EDS) attached to the scanning electron microscope. The crystal orientation of the electrodeposited samples was studied using an X-ray diffraction system (PANalytical X'Pert Pro) with Cu Kα radiation (α = 1.5406 Å) at a voltage of 40 kV and a current of 40 mA. The Raman spectra of the samples were recorded with a Renishaw (RA100) inVia confocal Raman microscope at 514.5 nm excitation.

The electrical transport and Hall properties were measured in a van der Pauw arrangement at room temperature under a magnetic field of 1.7 T on a 10 × 10 mm^2 thin film samples by using a Hall kit (Lakeshore model 8404). The Hall measurements are of above 99% accuracy. For the Seebeck coefficient measurements, a laboratory-built system was used. All the measurements were done in the in-plane orientation with different temperature gradients (ΔT), established along the ends of the samples using commercially available Peltier modules. The thermovoltage of the sample was measured over a range of ΔT values (2−10 °C) where the temperature was monitored using two separate thermocouples situated on either ends of the sample. The Seebeck coefficient was determined from the slope of the thermovoltage versus the temperature gradient. The measurement error is no more than 5% for this setup. Further details on the Seebeck coefficient measurements are provided in the Supporting Information. The presence of the Au seed layer underneath the deposited film and its impact on the thermoelectric and electrical property measurements of the film have been taken into consideration. However, telluride-based chalcogenides, such as BiTe alloys, demonstrate an anisotropic behavior with respect to thermal/electrical properties.[30,31] Hence, we think that it might be possible that the in-plane electrical resistivity is different compared to the cross-plane resistivity of the deposited material. The electrical resistivity was measured using an in-line four-point probe measurement system (Jandel RM3000), which was also used to cross-check the sheet resistance values obtained from the Hall measurements. The electrical conductivity values from both the techniques were almost the same within an error of 4%.

3. RESULTS AND DISCUSSION

3.1. Electrochemical Deposition. The electrolytic behavior of different baths was investigated using CV to understand the reduction mechanism of the electrolyte with Cu and Te ions. Three separate baths were prepared: the first bath with 2 mM copper (II) sulfate pentahydrate dissolved in 200 mL DI water, the second bath consisting of 15 mM tellurium in 1 M nitric acid; and the third bath with 2 mM copper (II) sulfate and 15 mM of tellurium in 1 M nitric acid. All the CV measurements were recorded using the standard gold electrode with respect to the Ag/AgCl reference electrode. Figure 1 shows the recorded cyclic voltammograms of the prepared baths. The CV from pure Cu bath depicts two cathodic and two anodic peaks, representing different reduction and oxidation states of Cu. One small and one broad reduction peaks are observed with the maximum current density at −40 and −217 mV, respectively. The former peak is due to the reduction of Cu^{2+} to Cu^{1+}, and the latter is due to the reduction of Cu^{1+} to metallic Cu^0.[32−34] The two oxidation peaks correspond to Cu^{1+} and Cu^{2+}, respectively.

$$Cu^{2+} + e \rightarrow Cu^{1+}(slow) \quad (1)$$

https://dx.doi.org/10.1021/acsaem.9b02153
ACS Appl. Energy Mater. XXXX, XXX, XXX−XXX

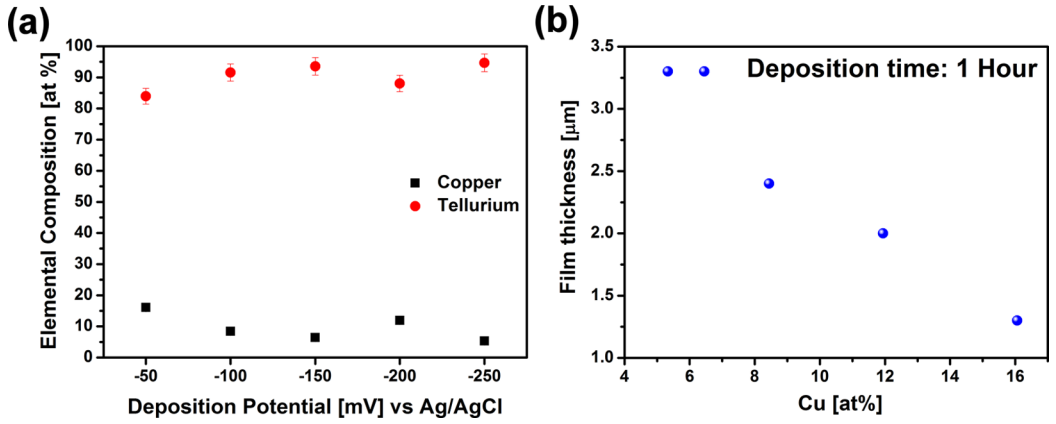

Figure 2. (a) Elemental composition of films at different deposition potentials and (b) thickness of electrodeposited films with different Cu atomic percentages.

$$Cu^{1+} + e \rightarrow Cu(fast) \quad (2)$$

Dissolution of Te in the nitric acid gives rise to $HTeO_2^+$ ions, and the recorded cyclic voltammogram of the bath has a single broad reduction peak with the peak current at −180 mV, resulting in the reduction of Te as depicted in eq 3 and a single oxidation peak at 510 mV.

$$HTeO_2^+ + 4e^- + 3H^+ \rightarrow Te + 2H_2O \quad (3)$$

The cyclic voltammogram recorded for the solution with 2 mM Cu and 15 mM Te in 1 M HNO_3 revealed a single broad peak at less negative potentials with the maximum cathodic current at −70 mV as depicted in Figure 1. The CV also reveals the oxidation peak at 510 mV and an overlapping shoulder peak corresponding to the oxidation of Te and Cu, respectively.

Five different potentials were selected in order to understand the role of the deposition potential on the stoichiometry of the films. All the films were deposited at a constant potential ranging from −50 to −250 mV with an interval of −50 mV.

The elemental composition of the films deposited at different potentials is shown in Figure 2a. The composition of the films varied with different deposition potentials as depicted in the figure. The film deposited at −50 mV led to a maximum Cu percentage in the films of 16.06%. Moreover, with an increase in the deposition potentials, the Cu content tends to decrease to 6.45% for the films deposited at −150 mV. On further increasing the deposition potential (at −200 mV), the Cu content increases and reaches to 11.94%. However, deposition at −250 mV resulted in a decrease in the Cu percentage as observed from EDS studies. This can be attributed to the Cu^{1+} reduction at a lower potential, leading to a higher Cu content in the films. Similarly, the reduction of Cu^{2+} ions to Cu is prominent at −200 mV, increasing the Cu reduction kinetics, thereby resulting in a higher Cu content. However, Te maintains significantly higher atomic percentages in the deposited films due to the higher ion concentration (15 mM) in the bath as compared to Cu with 2 mM concentration and due to the higher reduction current of Te as can be observed in Figure 1.

Figure 2b shows the detrimental effect on the deposition rate of the increase in the Cu content in the films. The films with less Cu have a higher deposition rate as compared to the films with the higher atomic percentage of Cu. This shows that the Cu content in the film hinders the kinetics of the film growth, resulting in a decrease in the deposition rates. This can be due to the formation of a higher nucleation site of Cu, hindering the deposition of Te.

3.2. Structural Properties. The micrographs of the films deposited at different deposition potentials were recorded as shown in Figure 3. From the micrographs, we can see that

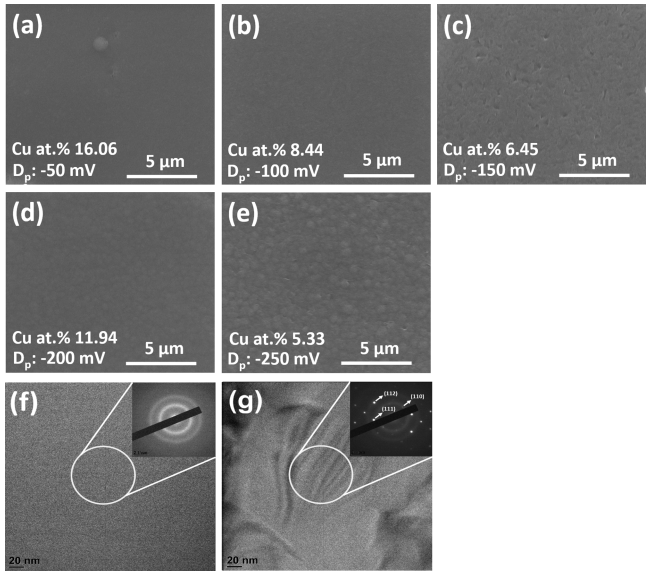

Figure 3. SEM and TEM micrographs of Cu-doped Te films at (a) −50, (b) −100, (c) −150, (d) −200, and (e) −250 mV. (f) TEM image of the film deposited at −50 mV with the SAED inset and (g) TEM image of the film deposited at −50 mV, showing nanofeatures along with the SAED inset.

there is no significant microstructure, revealing smooth and dense films. The films deposited at −100, −150, and −250 mV, which also tend to have a Cu at.% of 8.44%, 6.45%, and 5.33%, respectively, have a solid and visibly flat structure. However, there is no structure observed for the other films deposited at −50 and − 200 mV that have a higher Cu content of 16.06 and 11.94% as compared to the films deposited at other potentials. This study reveals that the Cu percentage in the films has a significant impact on the microstructure. To investigate further, a thorough TEM analysis was performed on the sample with the maximum Cu content at multiple places. TEM showed a highly amorphous structure with no crystallite

https://dx.doi.org/10.1021/acsaem.9b02153
ACS Appl. Energy Mater. XXXX, XXX, XXX−XXX

features, as shown in Figure 3f. The selected area electron diffraction (SAED) rings further confirms that the films are amorphous as can been seen in the Figure 3f inset. However, very few places in the sample showcased nanofeatures with no specific shapes. SAED was performed on these features. As expected, these features tend to be crystalline, and this is due to the presence of the $Cu_{2-x}Te$ phase, which was confirmed using SAED as shown in the inset of Figure 3g. In order to further investigate, X-ray diffraction (XRD) patterns of the films with increasing Cu at.% are plotted as shown in Figure 4.

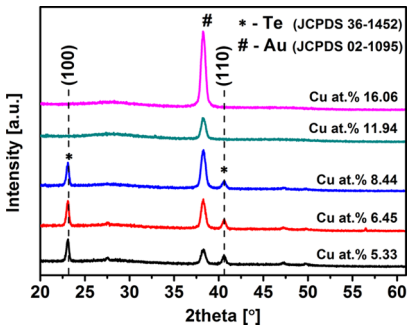

Figure 4. X-ray diffraction patterns of the deposited films with increasing Cu at.% in the films.

Diffraction peaks of (100, 110) are found for the films with Cu at.% < 11.94, and the observed diffraction peaks are indexed to a trigonal phase of tellurium (JCPDS 36-1452). The (100) diffraction peak located at 23.09 is the prominent peak for the films with Cu at.% of 5.33%, 6.45%, and 8.44%, and the peak at 2θ = 40.60 corresponds to the (110) crystallographic orientation. The Au diffraction peak (111) at 2θ = 38.25 originates from the Au seed layer used for the electrodeposition of the films. Even though the EDS shows a substantial presence of Cu in the films, the XRD patterns show no pattern of either elemental Cu or CuTe phases. However, with an increase in the Cu percentage above 8.44% in the film, the crystal structure drastically collapsed as no diffraction peaks are observed for the films, changing the films from crystalline to amorphous. The average crystallite size of different orientations is calculated using the Debye−Scherrer equation and shown in Table 1. With the increase of the Cu content in the films until 8.44%, no major change in the average crystallite size is observed for the peak with the (100) orientation. However, the crystallite size evaluated using the (110) orientation decreased with an increase of Cu percentage in the film, and finally, the films became amorphous.

Table 1. Average Crystallite Size of the Films with Increasing Cu at.% in the Films

		average crystallite size [nm]	
copper [at.%]	deposition potential [mV]	(100)	(110)
5.33	−250	26.45	20.10
6.45	−150	26.45	19.66
8.44	−100	25.65	17.01
11.94	−200	amorphous	amorphous
16.06	−50	amorphous	amorphous

Raman spectra were recorded using a Renishaw (RA100) with an excitation wavelength of 514 nm at 50× magnification at different positions on the films. The Lorentzian function was used to fit the spectra and to obtain the peak value. The spectra were recorded at different spots of the films to ensure the reproducibility. There was no change in the peak positions with measurements done at different spots on the films except for a nominal difference in the intensities. The Raman spectra were recorded for different concentrations of Cu in Te films as shown in Figure 5. Three prominent Raman peaks are observed at ∼92, ∼122, and 140 cm^{-1}. The Raman spectra for the Cu-doped Te films match with the spectrum of Te thin films.[35] However, the spectra do not match with $Cu_{2-x}Te$ films,[36,37] confirming no $Cu_{2-x}Te$ phase formation and is in agreement with our XRD data. The characteristic vibrational modes of different Te films from the literature and the films deposited in the present work are tabulated in Table 2.

As observed from Table 2, the Raman shift of tellurium films grown with different techniques has a spread in the recorded data. The most intense peak is located at ∼122 cm^{-1}, which can be attributed to the A^1 mode, corresponding to the chain expansion mode where each atom moves in the basal plane.[38,40] Meanwhile, there exist two degenerate E modes, which separate into predominately bond-bending and bond-stretching types. The E^1 mode at ∼92 cm^{-1} is caused by an *a*-axis rotation, and the E^2 mode at ∼140 cm^{-1} is attributed to asymmetric stretching mainly along the *c* axis[40] as depicted in Figure 5. In order to study the effect of Cu addition in Te films, the shift in the Raman peaks is plotted with respect to the Cu concentration in the films (Figure 5b). With the addition of Cu, the prominent A^1 peak moves to a higher Raman shift until the Cu concentration reaches 8.44% and does not change for the 11.94% Cu sample. In between these Cu concentrations, there is a transformation from the crystalline to the amorphous phase as observed from the XRD data (see Figure 4). Further addition of Cu in the films reduces the Raman peak shift. A similar trend is followed by all other vibration modes, as can be seen in Figure 5b. This shift to a higher frequency of Raman peak positions for Cu-doped samples (as compared to pure Te) shows that Cu interacts with the Te chemical bonds, which finally results in collapsing of the crystal structure. From our XRD studies, it is clear that the addition of Cu distorts the crystal structure, and after a particular concentration, the crystallinity diminishes with the films getting amorphous. However, the mechanism of how Cu initiates and participates in the crystal distortion and finally collapsing the crystal structure without forming any separate phase with Te is still not clear. Nevertheless, this amorphous nature of the material has a significant impact on the thermoelectric properties as discussed in the subsequent section.

3.3. Thermoelectric Properties. The thermoelectric properties of the electrodeposited films are investigated as a function of Cu concentration. Figure 6a shows the Seebeck coefficient and the electrical conductivities with respect to Cu at.% in the films. As discussed in the previous section, the Cu content in the film changes with the deposition potentials. This change in the Cu content has a direct impact on the thermoelectric properties of the electrodeposited films. The Seebeck coefficient of the films decreased with an increase in the Cu content in the films except for the films deposited at −50 mV, which also tend to have the maximum Cu content in the films. The film with a maximum Cu content of 16.06 at.% has a Seebeck coefficient of −227 μV/K.

The electrical conductivity of the films increased with the increase of the Cu concentration in the films as shown in

https://dx.doi.org/10.1021/acsaem.9b02153
ACS Appl. Energy Mater. XXXX, XXX, XXX−XXX

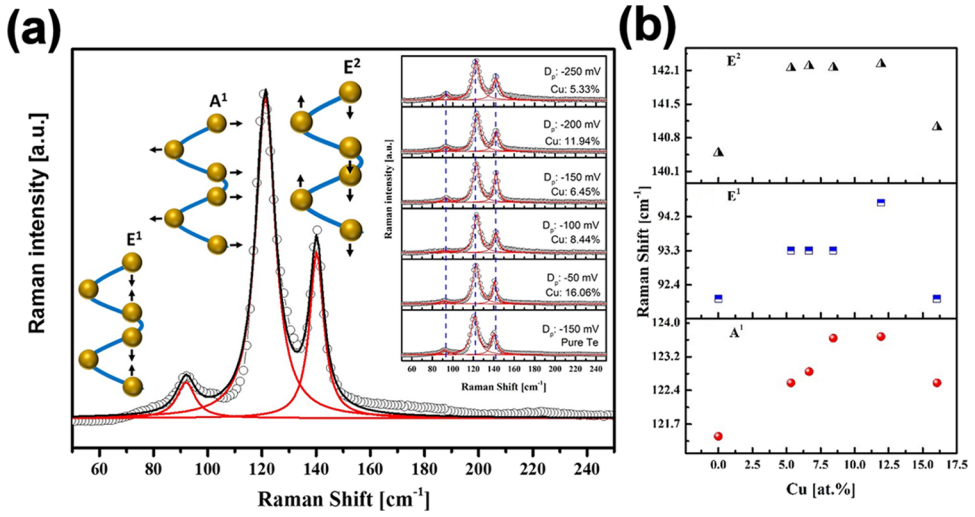

Figure 5. (a) Room temperature Raman scattering spectra of films without and with increasing Cu at.% in the films and (b) Raman spectra peak shift of A^1, E^1, and E^2 peaks.

Table 2. Tellurium Vibrational Modes Measured in Comparison with the Data Published in the Literature

	vibrational modes (cm^{-1})			
sample	E^1	A^1	E^2	reference
Cu-doped Te film	92	121.4	139.9	this work
Te cluster	93	123	142	36
1-D Te	94	122	142	38
Te film	88	117	137	39
Te film	91.3	119.7	139.5	35

Figure 6a. Addition of Cu enhances the electrical conductivity of the electrodeposited films, with the maximum conductivity achieved by films with 16.06 at.% of Cu. In order to understand the impact of the Cu content on thermoelectric properties of the films, electronic transport properties, carrier concentration, and mobility were measured using a Hall probe. All the measured Hall voltages were negative in sign, indicating electrons as the majority charge carriers and confirming the negative Seebeck coefficient. The interdependent relation between the Seebeck coefficient, the carrier densities, the mobility, and the electrical conductivity can be expressed by the following equations

$$S = \frac{8\pi^2 k_b^2}{3eh^2} \cdot m^* T \left(\frac{\pi}{3n}\right)^{2/3} \quad (4)$$

$$\frac{1}{\rho} = e \cdot n \cdot \mu \quad (5)$$

where n is the carrier density, k_b is the Boltzmann constant, e is the electron charge, h is the Planck constant, m^* is the charge carrier effective mass, and μ is the mobility.[14] Electrical resistivity (ρ) of the film can be decreased with high carrier concentrations as well as with an increase in the carrier mobility as expressed in eq 5.

The change in the carrier concentrations and the mobility of the films can be directly correlated with the Seebeck and electrical conductivities of the films with different Cu concentrations. Figure 6b shows the carrier concentration and mobility as a function of Cu concentration in the films. The mobility of the films initially increases from 0.25 to 1.8 cm^{2}V^{-1}s^{-1} for the films with 5.33 to 8.44 at.% of Cu. On further increase in the Cu content, at which the crystallinity of the films collapses, a sudden decrease in the mobility to 0.28 cm^{2}V^{-1}s^{-1} can be observed for the films with 11.94% Cu content. This decrease in mobility might have a direct relation

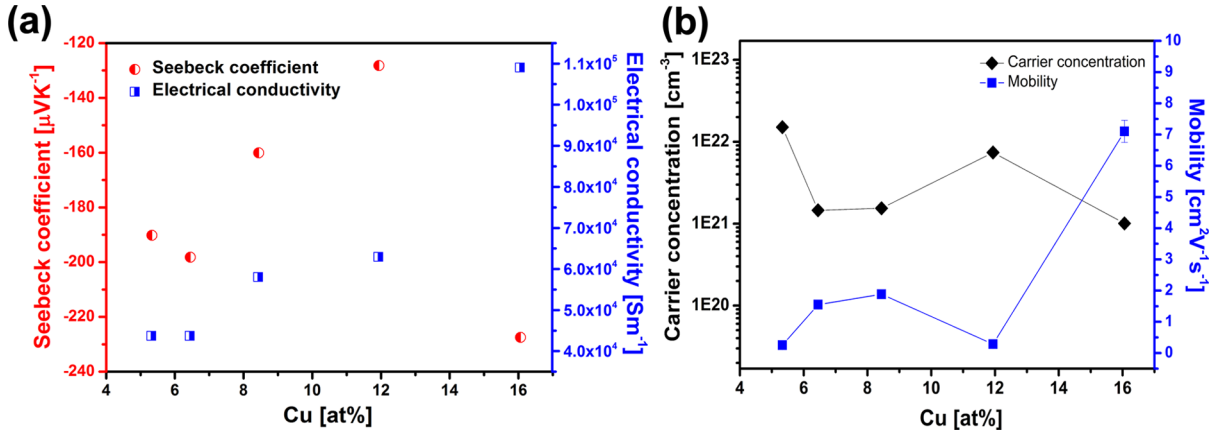

Figure 6. (a) Thermoelectric properties of electrodeposited Cu-doped Te films with different Cu contents in the films, and (b) mobility and carrier concentration as a function of Cu atomic percentage in the films.

https://dx.doi.org/10.1021/acsaem.9b02153
ACS Appl. Energy Mater. XXXX, XXX, XXX−XXX

with the collapse in crystallinity of the films. However, a further increase in the Cu content (16.06 at.%) resulted in a maximum mobility of 7.1 $cm^2V^{-1}s^{-1}$. The presence of nanocrystalline features in the sample with a Cu content of 16.06 at.% as observed in the TEM analysis shown in Figure 3g might be the reason for an increase in the mobility, which ultimately increased the overall electrical conductivity of the sample. On the other hand, the charge carrier concentration of the films does not show any drastic change as a function of Cu content in the films and stays within the range of 10^{14}−10^{22} cm^{-3}. The film with the maximum Cu content exhibits the lowest charge concentrations, which leads to high Seebeck coefficient values for the films.

The overall increase in the Seebeck coefficient and the electrical conductivity resulted in high power factors of Cu-doped Te films at room temperature. The films with the Cu content of ∼5−12 at.% have a power factor of ∼1−1.7 mW/mK^2, and the film with a high percentage of Cu showed a maximum power factor of 5.6 mW/mK^2 as shown in Figure 7,

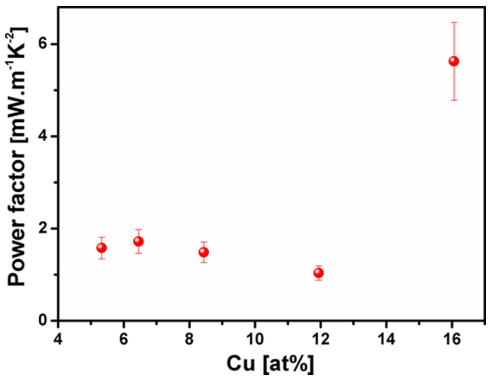

Figure 7. Calculated power factor of the films with different Cu at.% in the films.

which is the highest power factor obtained for an electrodeposited near-room temperature thermoelectric material. In comparison with thermoelectric materials synthesized using other deposition techniques, the obtained power factor of the Cu-doped Te-electrodeposited films stands out not only with Bi—Te-based thermoelectric materials but also with the CrN thin films, which have shown a promising thermoelectric performance near room temperature recently.[29,41] Further investigation on the temperature dependence of the thermoelectric properties of the deposited films is required to evaluate its application in future micro-thermoelectric devices for wider temperature range applications.

4. CONCLUSIONS

Cu-doped Te films with varying Cu contents were electrodeposited using different reduction potentials. Reduction of Cu, Te, and CuTe were studied using cyclic voltammetry. The Cu content has a significant impact on the structure of the electrodeposited films as well as on its thermoelectric performance. Increase of the Cu content over a certain range tends to destroy the crystallinity of the films, eventually making them amorphous. The as-deposited films show an n-type behavior with a maximum Seebeck coefficient of −227 μV/K, resulting in a power factor of 5.6 mW/mK^2, which is one of the most promising power factor values as compared to the reported contemporary electrodeposited room-temperature thermoelectric material.

■ ASSOCIATED CONTENT

Supporting Information

The Supporting Information is available free of charge at https://pubs.acs.org/doi/10.1021/acsaem.9b02153.

Seebeck coefficient measurement setup and working principle, raw data of the thermovoltage versus temperature gradient of the electrodeposited samples, re-measurement of the −50 mV-deposited sample eight months after the film deposition, RMS roughness analysis on the films using AFM measurements, and reproducibility study of the −50 mV-deposited sample (PDF)

■ AUTHOR INFORMATION

Corresponding Authors

Kafil M. Razeeb − *Micro-Nano Systems Centre, Tyndall National Institute, University College Cork, Cork T12 R5CP, Ireland*; orcid.org/0000-0001-9360-9277; Email: kafil.mahmood@tyndall.ie

Devendraprakash Gautam − *Micro-Nano Systems Centre, Tyndall National Institute, University College Cork, Cork T12 R5CP, Ireland*; Email: gautam3000in@gmail.com

Author

Swatchith Lal − *Micro-Nano Systems Centre, Tyndall National Institute, University College Cork, Cork T12 R5CP, Ireland*; orcid.org/0000-0001-5351-7722

Complete contact information is available at: https://pubs.acs.org/10.1021/acsaem.9b02153

Funding

This work has received funding from the European Union's Horizon 2020-funded project under grant agreement no. 825114 (SmartVista). Authors also acknowledge the support by the Science Foundation Ireland (SFI) through SFI grants 15/IA/3160 and 12/RC/2276.

Notes

The authors declare no competing financial interest.

■ REFERENCES

(1) Du, L.; Shi, G.; Zhao, J. Review of micro magnetic generator. *Sens. Transducers* **2014**, *176*, 1−12.

(2) Calhoun, B. H.; Daly, D. C.; Verma, N.; Finchelstein, D. F.; Wentzloff, D. D.; Wang, A.; Cho, S.-H.; Chandrakasan, A. P. Design considerations for ultra-low energy wireless microsensor nodes. *IEEE Trans. Comput.* **2005**, *54*, 727−740.

(3) Haras, M.; Skotnicki, T. Thermoelectricity for IoT − A review. *Nano Energy* **2018**, *54*, 461−476.

(4) Rabaey, J. M.; Ammer, J.; Karalar, T.; Suetfei, L.; Otis, B.; Sheets, M.; Tuan, T. PicoRadios for wireless sensor networks: the next challenge in ultra-low power design. In *2002 IEEE International Solid-State Circuits Conference. Digest of Technical Papers (Cat. No.02CH37315)*; IEEE: 7−7 Feb. 2002; 2002; pp 200−201 vol.1.

(5) Arnold, D. P. Review of Microscale Magnetic Power Generation. *IEEE Trans. Magn.* **2007**, *43*, 3940−3951.

(6) Selvan, K. V.; Mohamed Ali, M. S. Micro-scale energy harvesting devices: Review of methodological performances in the last decade. *Renewable Sustainable Energy Rev.* **2016**, *54*, 1035−1047.

(7) Dahiya, A. S.; Thireau, J.; Boudaden, J.; Lal, S.; Gulzar, U.; Zhang, Y.; Gil, T.; Azemard, N.; Ramm, P.; Kiessling, T.; O'Murchu, C.; Sebelius, F.; Tilly, J.; Glynn, C.; Geary, S.; O'Dwyer, C.; Razeeb,

K. M.; Lacampagne, A.; Charlot, B.; Todri-Sanial, A., Review—Energy Autonomous Wearable Sensors for Smart Healthcare: A Review. *J. Electrochem. Soc.* **2020**, *167* (), DOI: 10.1149/2.0162003JES.
(8) Fleurial, J.-P.; Snyder, G. J.; Herman, J. A.; Giauque, P. H.; Phillips, W. M.; Ryan, M. A.; Shakkottai, P.; Kolawa, E. A.; Nicolet, M. A. Thick-film thermoelectric microdevices. In *Thermoelectrics, 1999. Eighteenth International Conference on*; IEEE: Aug. 29 1999-Sept. 2 1999; 1999; pp 294−300.
(9) Lal, S.; Gautam, D.; Razeeb, K. M. Fabrication of micro-thermoelectric devices for power generation and the thermal management of photonic devices. *J. Micromech. Microeng.* **2019**, *29*, No. 065015.
(10) Snyder, G. J.; Lim, J. R.; Huang, C.-K.; Fleurial, J.-P. Thermoelectric microdevice fabricated by a MEMS-like electrochemical process. *Nat. Mater.* **2003**, *2*, 528−531.
(11) Dunham, M. T.; Barako, M. T.; LeBlanc, S.; Asheghi, M.; Chen, B.; Goodson, K. E. Power density optimization for micro thermoelectric generators. *Energy* **2015**, *93*, 2006−2017.
(12) Witting, I. T.; Chasapis, T. C.; Ricci, F.; Peters, M.; Heinz, N. A.; Hautier, G.; Snyder, G. J. The Thermoelectric Properties of Bismuth Telluride. *Adv. Electron. Mater.* **2019**, *5*, 1800904.
(13) Lal, S.; Gautam, D.; Razeeb, K. M. Optimization of annealing conditions to enhance thermoelectric performance of electrodeposited p-type BiSbTe thin films. *APL Mater.* **2019**, *7*, No. 031102.
(14) Snyder, G. J.; Toberer, E. S. Complex thermoelectric materials. *Nat. Mater.* **2008**, *7*, 105−114.
(15) Sootsman, J. R.; Chung, D. Y.; Kanatzidis, M. G. New and old concepts in thermoelectric materials. *Angew. Chem., Int. Ed.* **2009**, *48*, 8616−8639.
(16) Liu, H.; Yuan, X.; Lu, P.; Shi, X.; Xu, F.; He, Y.; Tang, Y.; Bai, S.; Zhang, W.; Chen, L.; Lin, Y.; Shi, L.; Lin, H.; Gao, X.; Zhang, X.; Chi, H.; Uher, C. Ultrahigh Thermoelectric Performance by Electron and Phonon Critical Scattering in Cu2Se1-xIx. *Adv. Mater.* **2013**, *25*, 6607−6612.
(17) Ge, Z.-H.; Zhang, B.-P.; Chen, Y.-X.; Yu, Z.-X.; Liu, Y.; Li, J.-F. Synthesis and transport property of Cu1.8S as a promising thermoelectric compound. *Chem. Commun.* **2011**, *47*, 12697−12699.
(18) He, Y.; Day, T.; Zhang, T.; Liu, H.; Shi, X.; Chen, L.; Snyder, G. J. High Thermoelectric Performance in Non-Toxic Earth-Abundant Copper Sulfide. *Adv. Mater.* **2014**, *26*, 3974−3978.
(19) He, Y.; Zhang, T.; Shi, X.; Wei, S.-H.; Chen, L. High thermoelectric performance in copper telluride. *NPG Asia Mater.* **2015**, *7*, No. e210.
(20) Qiu, P.; Shi, X.; Chen, L. Cu-based thermoelectric materials. *Energy Storage Mater.* **2016**, *3*, 85−97.
(21) Pei, Y.; Shi, X.; Lalonde, A.; Wang, H.; Chen, L.; Snyder, G. J. Convergence of electronic bands for high performance bulk thermoelectrics. *Nature* **2011**, *473*, 66−69.
(22) Hinterleitner, B.; Knapp, I.; Poneder, M.; Shi, Y.; Müller, H.; Eguchi, G.; Eisenmenger-Sittner, C.; Stöger-Pollach, M.; Kakefuda, Y.; Kawamoto, N.; Guo, Q.; Baba, T.; Mori, T.; Ullah, S.; Chen, X.-Q.; Bauer, E. Thermoelectric performance of a metastable thin-film Heusler alloy. *Nature* **2019**, *576*, 85−90.
(23) Zhao, L.-D.; Dravid, V. P.; Kanatzidis, M. G. The panoscopic approach to high performance thermoelectrics. *Energy Environ. Sci.* **2014**, *7*, 251−268.
(24) Yang, L.; Chen, Z.-G.; Dargusch, M. S.; Zou, J. High Performance Thermoelectric Materials: Progress and Their Applications. *Adv. Energy Mater.* **2018**, *8*, 1701797.
(25) He, R.; Schierning, G.; Nielsch, K. Thermoelectric Devices: A Review of Devices, Architectures, and Contact Optimization. *Adv. Mater. Technol.* **2018**, *3*, 1700256.
(26) Liu, W.; Kim, H. S.; Jie, Q.; Ren, Z. Importance of high power factor in thermoelectric materials for power generation application: A perspective. *Scr. Mater.* **2016**, *111*, 3−9.
(27) Hatsuta, N.; Takemori, D.; Takashiri, M. Effect of thermal annealing on the structural and thermoelectric properties of electrodeposited antimony telluride thin films. *J. Alloys Compd.* **2016**, *685*, 147−152.
(28) Zhou, J.; Wang, H.; He, D.; Zhou, Y.; Peng, W.; Fan, F.; Huang, H. Transferable and flexible thermoelectric thin films based on elemental tellurium with a large power factor. *Appl. Phys. Lett.* **2018**, *112*, 243904.
(29) Gharavi, M. A.; Kerdsongpanya, S.; Schmidt, S.; Eriksson, F.; Nong, N. V.; Lu, J.; Balke, B.; Fournier, D.; Belliard, L.; le Febvrier, A.; Pallier, C.; Eklund, P. Microstructure and thermoelectric properties of CrN and CrN/Cr2N thin films. *J. Phys. D: Appl. Phys.* **2018**, *51*, 355302.
(30) Manzano, C. V.; Abad, B.; Muñoz Rojo, M.; Koh, Y. R.; Hodson, S. L.; Lopez Martinez, A. M.; Xu, X.; Shakouri, A.; Sands, T. D.; Borca-Tasciuc, T.; Martin-Gonzalez, M. Anisotropic Effects on the Thermoelectric Properties of Highly Oriented Electrodeposited Bi2Te3 Films. *Sci. Rep.* **2016**, *6*, 19129.
(31) Yan, X.; Poudel, B.; Ma, Y.; Liu, W. S.; Joshi, G.; Wang, H.; Lan, Y.; Wang, D.; Chen, G.; Ren, Z. F. Experimental Studies on Anisotropic Thermoelectric Properties and Structures of n-Type Bi2Te2.7Se0.3. *Nano Lett.* **2010**, *10*, 3373−3378.
(32) Pasquale, M. A.; Gassa, L. M.; Arvia, A. J. Copper electrodeposition from an acidic plating bath containing accelerating and inhibiting organic additives. *Electrochim. Acta* **2008**, *53*, 5891−5904.
(33) Gabrielli, C.; Moçotéguy, P.; Perrot, H.; Nieto-Sanz, D.; Zdunek, A. An investigation of copper interconnect deposition bath ageing by electrochemical impedance spectroscopy. *J. Appl. Electrochem.* **2008**, *38*, 457−468.
(34) Vazquez-Arenas, J.; Cruz, R.; Mendoza-Huizar, L. H. The role of temperature in copper electrocrystallization in ammonia−chloride solutions. *Electrochim. Acta* **2006**, *52*, 892−903.
(35) Torrie, B. H. Raman spectrum of tellurium. *Solid State Commun.* **1970**, *8*, 1899−1901.
(36) Salmón-Gamboa, J. U.; Barajas-Aguilar, A. H.; Ruiz-Ortega, L. I.; Garay-Tapia, A. M.; Jiménez-Sandoval, S. J. Vibrational and electrical properties of Cu2−xTe films: experimental data and first principle calculations. *Sci. Rep.* **2018**, *8*, 8093.
(37) Dhasade, S. S.; Han, S. H.; Fulari, V. J. A nanostructured copper telluride thin film grown at room temperature by an electrodeposition method. *J. Semicond.* **2012**, *33*, No. 093002.
(38) Du, Y.; Qiu, G.; Wang, Y.; Si, M.; Xu, X.; Wu, W.; Ye, P. D. One-Dimensional van der Waals Material Tellurium: Raman Spectroscopy under Strain and Magneto-Transport. *Nano Lett.* **2017**, *17*, 3965−3973.
(39) Rodríguez-Fernández, C.; Manzano, C. V.; Romero, A. H.; Martín, J.; Martín-González, M.; de Lima, M. M., Jr.; Cantarero, A. The fingerprint of Te-rich and stoichiometric Bi_2Te_3 nanowires by Raman spectroscopy. *Nanotechnology* **2016**, *27*, No. 075706.
(40) Martin, R. M.; Lucovsky, G.; Helliwell, K. Intermolecular bonding and lattice dynamics of Se and Te. *Phys. Rev. B* **1976**, *13*, 1383−1395.
(41) Yan, J.; Liao, X.; Yan, D.; Chen, Y. Review of Micro Thermoelectric Generator. *J. Microelectromech. Syst.* **2018**, *27*, 1−18.

https://dx.doi.org/10.1021/acsaem.9b02153
ACS Appl. Energy Mater. XXXX, XXX, XXX−XXX